ADVANCED FUNCTIONAL MATERIALS
www.afm-journal.de

Enhancement in Organic Photovoltaic Efficiency through the Synergistic Interplay of Molecular Donor Hydrogen Bonding and π-Stacking

Nathan T. Shewmon, Davita L. Watkins, Johan F. Galindo, Raghida Bou Zerdan, Jihua Chen, Jong Keum, Adrian E. Roitberg, Jiangeng Xue, and Ronald K. Castellano**

For organic photovoltaic (OPV) cells based on the bulk heterojunction (BHJ) structure, it remains challenging to rationally control the degree of phase separation and percolation within blends of donors and acceptors to secure optimal charge separation and transport. Reported is a bottom-up, supramolecular approach to BHJ OPVs wherein tailored hydrogen bonding (H-bonding) interactions between π-conjugated electron donor molecules encourage formation of vertically aligned donor π-stacks while simultaneously suppressing lateral aggregation; the programmed arrangement facilitates fine mixing with fullerene acceptors and efficient charge transport. The approach is illustrated using conventional linear or branched quaterthiophene donor chromophores outfitted with terminal functional groups that are either capable or incapable of self-complementary H-bonding. When applied to OPVs, the H-bond capable donors yield a twofold enhancement in power conversion efficiency relative to the comparator systems, with a maximum external quantum efficiency of 64%. H-bond promoted assembly results in redshifted absorption (in neat films and donor:C_{60} blends) and enhanced charge collection efficiency despite disparate donor chromophore structure. Both features positively impact photocurrent and fill factor in OPV devices. Film structural characterization by atomic force microscopy, transmission electron microscopy, and grazing incidence wide angle X-ray scattering reveals a synergistic interplay of lateral H-bonding interactions and vertical π-stacking for directing the favorable morphology of the BHJ.

1. Introduction

Photovoltaic (PV) cells based on π-conjugated organic materials have generated significant interest due to their low materials costs and flexible, thin film device architectures.[1–6] Constructs of the most efficient organic photovoltaic (OPV) cells often rely on a bulk heterojunction (BHJ) photoactive layer consisting of a blend of an electron donor (typically a π-conjugated molecule or polymer) and acceptor (typically a fullerene), the morphology of which controls the generation and transport of charge carriers.[7,8] Securing a desired BHJ morphology is typically left to chance and is strongly, but not usually predictably, dependent on donor and acceptor molecular structure as well as processing methods and conditions. While some control of the phase separation process can be realized through solvent additives[9–11] and/or postdeposition treatments (e.g., solvent and thermal annealing),[7] still highly sought are general molecular-level design approaches to improve BHJ morphology rationally across structurally distinct families of donors and/or acceptors for further improvement in OPV efficiency. To date, fluorination of the donor component remains one of the few structural modifications that have boasted universal advantages.[12–26] Herein, we illustrate an approach based on the hydrogen bond directed self-assembly of molecular donors that improves absorption and charge collection for BHJ OPVs irrespective of donor molecular structure.

Supramolecular organization driven by H-bonding as a way to tailor BHJ morphology and optimize OPV performance has gained momentum in recent years. The approach, on one hand, is logical since H-bonds are well established for controlling the structures of π-systems in solution and the solid state,[27,28] function cooperatively with π-stacking interactions, and can lead to improved long-range ordering, charge carrier mobility, and stability in device active layers of neat π-conjugated materials (e.g., organic field effect transistors).[29–45] On the other hand,

Dr. N. T. Shewmon, Prof. J. Xue
Department of Materials Science and Engineering
University of Florida
P.O. Box 116400, 32611-6400, Gainesville, FL, USA
E-mail: jxue@mse.ufl.edu
Dr. D. L. Watkins, Dr. J. F. Galindo, R. B. Zerdan, Prof. A. E. Roitberg, Prof. R. K. Castellano
Department of Chemistry
University of Florida
P.O. Box 117200, 32611-7200, Gainesville, FL, USA
E-mail: castellano@chem.ufl.edu
Dr. J. Chen, Dr. J. Keum
Center for Nanophase Materials Sciences
Oak Ridge National Laboratory
Oak Ridge, 37831-6496 TN, USA

DOI: 10.1002/adfm.201501815

to what extent H-bonding might be universally advantageous in the more complex two-component BHJ OPV environment is unclear, and literature reports suggest that the outcomes are mixed and design dependent. For the systems involving self-complementary H-bonding interactions between molecular donors (in the presence of fullerene acceptors), including our own,[46] improvements in crystallinity, V_{OC}, fill factor (FF), and power conversion efficiency (PCE) have been noted.[47–54] However, H-bonding has been linked to diminished OPV performance as a consequence of unfavorable BHJ morphology in nearly as many scenarios.[52,55–58] While the results when taken together are encouraging, additional work is needed to identify contexts wherein H-bond directed assembly of molecular OPV donors leads to persistent enhancements in the optical and electrical properties of the BHJ OPV active layer.

Mentioned above, we recently performed a systematic molecular structure–property relationship study evaluating the consequences of H-bonding interactions between molecular electron donors based on branched quaterthiophene (BQ) chromophores on thin film morphology, absorption, charge collection, and performance in BHJ OPVs.[46] In the work, we specifically probed the role of H-bonded assembly of phthalhydrazide (PH)-functionalized branched quaterthiophene (MeBQPH, see **Figure 1**) on OPV performance through comparison to two molecules of similar size, shape, and electronic structure that are incapable of H-bonding (e.g., MeBQPME). The self-complementary H-bonding occurs through the lactim–lactam tautomer of the phthalhydrazide heterocycle that can facilitate the formation of linear and cyclic H-bonded assemblies.[59–61] Implicated in the work, and since confirmed in solution by DOSY NMR,[62] on Au(111) surfaces by scanning tunneling microscopy (STM),[63] and in the gas phase through density functional theory (DFT) calculations,[63] is the propensity for PH to form stable trimer rosettes (i.e., $(PH)_3$). OPV devices showed doubled charge collection length, enhanced and redshifted absorption, and improved external quantum efficiency (EQE) for MeBQPH relative to MeBQPME, resulting in a more than twofold enhancement in power conversion efficiency. As best as our studies could ascertain, the performance improvements came as a consequence of H-bond promoted molecular packing.

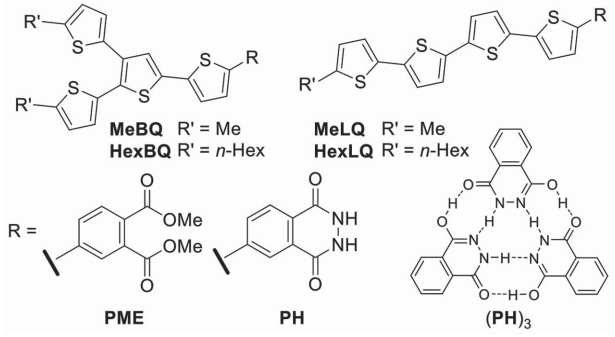

Figure 1. Molecular structures of the oligothiophenes (BQ, branched quaterthiophene; LQ, linear quaterthiophene) discussed in this work that are either capable (PH) or incapable (PME) of hydrogen bond directed self-assembly. Also shown is trimer rosette formation from phthalhydrazide (PH), a mode of association that has been characterized on surfaces for MeBQPH and in solution for HexBQPH (see text for details).

In this current work, we exploit the modularity of our molecular design to evaluate whether the H-bond associated enhancement in OPV performance realized for MeBQPH can be reproduced in the context of a different molecular donor. To this end, we have replaced the BQ chromophore with a pseudo-isomeric linear quaterthiophene (LQ) which has the additional advantages of stronger π-stacking due to a largely planar molecular shape, a reduced optical gap, and more optimal light absorbing properties. The new molecules considered here through experimental and theoretical studies, H-bond capable LQPH and H-bond incapable comparator LQPME, are illustrated in Figure 1. Detailed comparison—particularly with respect to thin film optoelectronic properties, morphology, and BHJ OPV device performance—between the LQPH/LQPME and BQPH/BQPME families, provides the most conclusive evidence to date that appropriately positioned H-bonding between molecular OPV donors can systematically improve BHJ morphology and OPV device performance due to synergistic interplay between in-plane H-bonding and out-of-plane π-stacking.

2. Results and Discussion

2.1. Synthesis

The syntheses of MeBQPH and MeBQPME were described in our earlier work.[46] Preparation of HexLQPH and HexLQPME was achieved as shown in **Scheme 1**. Dimethyl 4-bromophthalate **1** could be prepared from the corresponding commercially available phthalic anhydride via acid catalyzed methanolysis.[46] Subsequent Stille coupling with 2-(tributylstannyl)thiophene provided dimethyl 4-(thiophen-2-yl)phthalate **2** which was brominated with NBS to afford **3**. The sequence, Stille coupling and halogenation, was repeated to provide **4** and **5**, respectively. Suzuki cross-coupling between **5** and commercially available 5′-hexyl-2,2′-bithiophene-5-boronic acid pinacol ester **6** yielded the comparator target, HexLQPME. Final condensation with hydrazine gave the H-bonding capable target phthalhydrazide, HexLQPH.

2.2. Optoelectronic Properties in the Molecularly Dissolved State

To confirm that the intrinsic optical and electrochemical properties of the targets were minimally different, HexLQPME and HexLQPH were studied in dilute DMF solution via UV–vis spectroscopy and differential pulse voltammetry (DPV). A summary of the optoelectronic properties is provided in **Table 1**. No aggregation via intermolecular H-bonding is expected under the measurement conditions. As shown in **Figure 2**a, the HexLQ molecules possess a very similar absorption profile with λ_{max} = 426–428 nm and λ_{onset} = 496–502 nm. The linear quaterthiophenes do, however, display redshifted absorption maxima and onsets (by 32–35 nm) compared to the branched series, a consequence of the thiophene connectivity and planarity (vide infra). DPV measurements (in DMF) show that HexLQPME and HexLQPH have nearly identical oxidation potentials (vs Fc/Fc^+). These values, determined from the oxidation onsets,

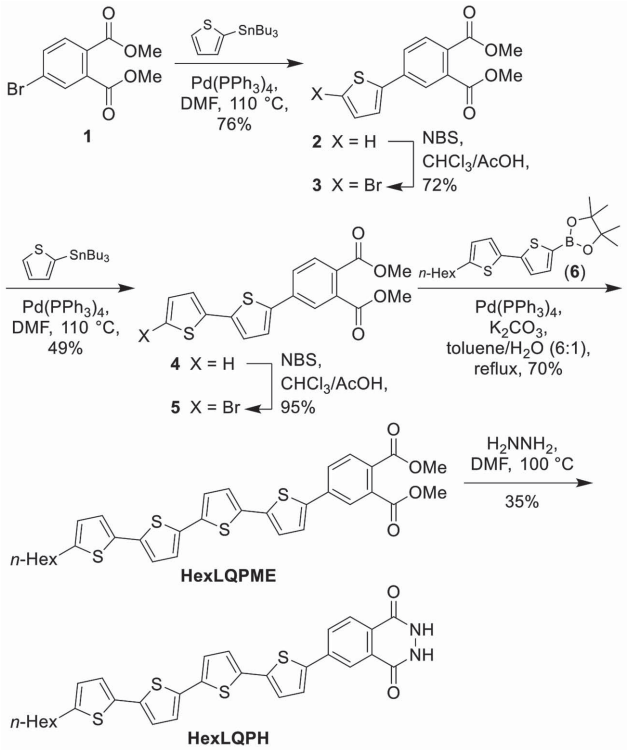

Scheme 1. Synthesis of HexLQPME and HexLQPH.

have been converted to HOMO energies for comparison (see Table S1 and Figures S1–S4 in the Supporting Information for details). Compared to the BQ series, the LQ congeners have slightly higher lying HOMO levels (by ≈0.2 eV) and slightly lower lying LUMO levels, in good overall agreement with the absorption data.

DFT calculations (B3LYP/6-31+G*) were used to identify the lowest energy forms, in terms of tautomer and conformational structure, of the BQ and LQ molecules (details are provided in the Experimental Section and the Supporting Information) in the molecularly dispersed state. For the calculations, the hexyl group of HexLQPH and HexLQPME was abbreviated to a methyl group to reduce computational cost (the compounds are shown in Figure 1 as MeLQPH and MeLQPME). For both MeBQPH and MeLQPH the predicted low-energy tautomer (in DMF) is the NH/NH form (as it is drawn for PH in Figure 1), that is 1.1 kcal mol^{-1} lower in energy than the next closest NH/OH form. Most gratifyingly, the calculations confirm the nearly identical electronic structures of the PH and PME derivatives within each family (Table 1). Consistent with the electrochemical data, calculations also predict that the LQ derivatives have slightly higher lying HOMO levels (by ≈0.2 eV) and slightly lower lying LUMO levels than the BQ compounds. Overall, the HOMO–LUMO gap trends are consistent across the experimental and theoretical data and predict an ≈0.2 eV gap reduction for the LQ series as compared to the corresponding BQ molecules. Shown in **Figure 3** are the HOMO and LUMO density plots for the BQ and LQ compounds; in both families the HOMO is localized on the oligothiophene portion and the LUMO is delocalized to include the modestly electron deficient PH and PME groups. Also evident from the molecular calculations (see the Supporting Information for additional graphics) are the differences in planarity between the BQ and LQ components. The most deviant S—C—C—S dihedral angle defined by α-linked thiophenes in MeBQPH is 131°; the angle in MeLQPH is a more planar 166°.

2.3. Neat and Blended Thin Film Optoelectronic Properties

Solid-state thin films were prepared from HexLQPME and HexLQPH by vacuum thermal evaporation. We note that the solubility of HexLQPME and HexLQPH in organic solvents, while sufficient for absorption characterization at 1×10^{-4} M, was not sufficient for solution processing of thin films by spin-coating. Absorption spectra of neat films (Figure 2a) show onset wavelengths of 527 and 549 nm, respectively, redshifted relative to the solution spectra by 31 and 47 nm. The larger redshift in absorption onset for HexLQPH (vs HexLQPME) is consistent with its tighter π–π stacking which comes, in large part (based on our previous studies,[46] from H-bonding mediated organization of the molecules. The neat thin film absorption onsets are also redshifted by 23–25 nm when compared to the BQ films, a result that transfers to thin film blends and has a bearing on overall OPV performance (vide infra). Gaussian fits to the absorption spectra of neat HexLQPH and HexLQPME

Table 1. Optical and electrochemical data for HexLQPH, HexLQPME, MeBQPH, and MeBQPME.

Donor	UV–vis (solution)[a]			UV–vis (neat films)[b]			DPV[c]			DFT calculations[d]		
	λ_{max} [nm]	λ_{onset} [nm]	$\Delta E_{g\text{-}opt}$ [eV]	λ_{max} [nm]	λ_{onset} [nm]	$\Delta E_{g\text{-}opt}$ [eV]	HOMO [eV]	LUMO [eV]	$\Delta E_{g\text{-}echem}$ [eV]	HOMO [eV]	LUMO [eV]	$\Delta E_{g\text{-}calcd}$ [eV]
HexLQPH	428	502	2.47	428	549	2.26	–5.41	–[f]	–[f]	–5.27	–2.60	2.67
HexLQPME	426	496	2.50	394	527	2.35	–5.44	–3.32	2.12	–5.27	–2.59	2.68
MeBQPH[e]	396	467	2.65	431	524	2.37	–5.63	–[f]	–[f]	–5.48	–2.51	2.97
MeBQPME[e]	392	464	2.67	414	504	2.46	–5.61	–3.25	2.37	–5.48	–2.50	2.98

[a]Absorbance data from DMF solution (1×10^{-4} M; 1 mm cell); optical gap ($E_{g\text{-}opt}$) determined from the absorption onset (λ_{onset}); [b]Absorbance data from 20 nm thick films; optical gap ($\Delta E_{g\text{-}opt}$) determined from the absorption onset (λ_{onset}); [c]Estimates of the HOMO and LUMO values (relative to vacuum), and corresponding energy gap ($\Delta E_{g\text{-}echem}$), derived from DPV experiments in DMF (0.1 M $TBAPF_6$) based on electrochemical potentials ($E_{ox\text{-}onset}$ and $E_{red\text{-}onset}$, respectively); [d]HOMO/LUMO energies and HOMO–LUMO energy gaps ($\Delta E_{g\text{-}calcd}$) obtained from DFT (B3LYP/6-31*G+) optimized structures in DMF (PCM model). MeLQPH and MeLQPME have been used for the calculations; [e]The experimental data were reported in a previous publication;[46] [f]Reproducible electrochemical data were not obtained for the PH derivatives at negative potentials.

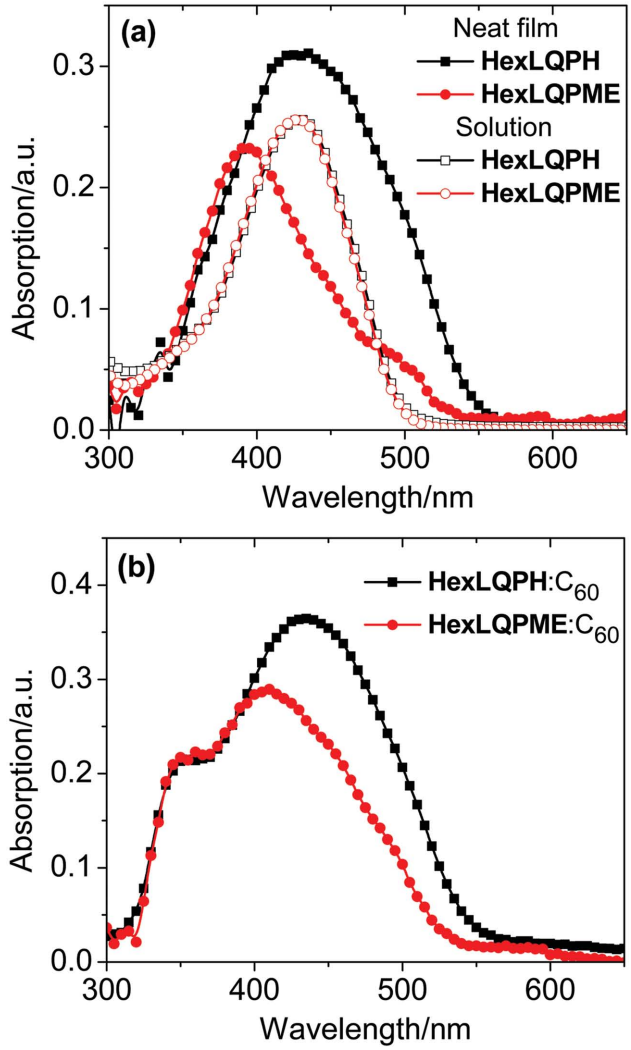

Figure 2. a) UV–vis absorbance spectra of HexLQPH and HexLQPME from 1×10^{-4} M DMF solution (open symbols) and absorptance spectra of 20–30 nm thick neat films (filled symbols), and b) absorptance spectra of 40–50 nm thick films blended 3:2 (by weight) with C_{60}.

films (Figure S5 and Table S2 in the Supporting Information) give some insight into the differences in molecular organization that result from the molecules. First, the lowest energy peak from fitting, which we tentatively assign to quaterthiophene π–π stacking, is located at 2.57 eV for HexLQPH and 2.51 eV for HexLQPME. While this peak is centered at nearly the same energy for both molecules, the peak height is fivefold to sixfold greater for HexLQPH films, suggesting that a greater fraction of the probed molecules are organized in π-stacks when H-bonding is present. Additionally, we note that the absorption maximum for the neat HexLQPME film is blueshifted by 32 nm relative to the molecularly dissolved state to 394 nm (3.15 eV), while the spectrum also shows longer wavelength shoulders which fit well to Gaussian peaks centered at 2.72 and 2.51 eV (456 and 494 nm, respectively). The blueshifted absorption maximum may be indicative of H-type aggregation in which molecular transition dipoles are arranged parallel to one another.[64] In the case of HexLQPH, a blueshift

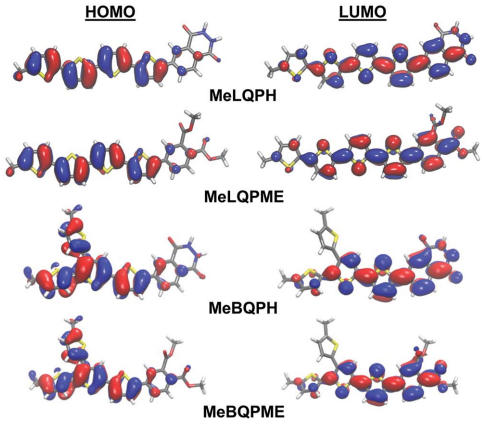

Figure 3. HOMO and LUMO density plots derived from DFT calculations (B3LYP/6-31+G*) for the BQ and LQ molecules in DMF (PCM); the lowest energy forms of the molecules are shown with respect to tautomer structure and conformation.

in maximum absorbance is not observed, indicating a difference in the mode of aggregation as a result of H-bond directed assembly.

The absorption spectra of 40 nm thick blended films (3:2 by weight) of HexLQPH:C_{60} and HexLQPME:C_{60} are shown in Figure 2b. Although the weak absorption of C_{60} out to >600 nm complicates the precise determination of the absorption onset, we obtain values of 546 and 525 nm for HexLQPH:C_{60} and HexLQPME:C_{60}, respectively, closely matching the values obtained for neat films. For MeBQPH:C_{60} and MeBQPME:C_{60} films, we previously determined[46] absorption onsets of 514 and 497 nm, respectively, which are blueshifted by 10 and 7 nm, respectively, from the corresponding neat film absorption onsets. Hence, we conclude that the addition of C_{60} does not disrupt the molecular aggregation that gives rise to a redshifted absorption onset for either HexLQPH or HexLQPME, and the stacking of more planar LQ molecules appears to be less disrupted by the presence of C_{60} than was the case for the less planar BQ molecules. Additional evidence for the preservation of donor structure in the presence of C_{60} is offered through IR spectroscopy (vide infra).

2.4. Signatures of H-Bonded Assembly

Due to the insolubility of HexLQPH, direct probing of H-bonding via ^{1}H NMR in solution was not possible. Fortunately, signatures of H-bonding were identified directly from FT-IR spectra of neat and blended thin films (Figure S6, Supporting Information) on NaCl substrates, consistent with our earlier studies with MeBQPH.[46] Upon H-bonding, the lactim–lactam tautomer of the parent PH (Figure 1) exhibits a single carbonyl stretch at 1662 cm^{-1} along with broadened N—H/O—H stretches up to 3600 cm^{-1}.[65] Likewise, MeBQPH shows similar features including a $\upsilon_{C=O}$ of 1659 cm^{-1} which is essentially unchanged from neat to blended films. As shown in Figure S6 (Supporting Information), both neat and blended (3:2 blend ratio by weight) films of HexLQPH are nearly identical, and show broadened resonances from 2700

to 3500 cm^{-1} as well as $\upsilon_{C=O} \approx 1660\ cm^{-1}$. As best as we can tell, H-bonding in the PH derivatives is sufficiently strong to persist in neat and mixed films. The consequences of H-bonded aggregation are indirectly evident from differential scanning calorimetry (DSC) which reveals (Figures S7 and S8, Supporting Information) a high melting transition (309 °C) for HexLQPH relative to HexLQPME (218 °C). Also worth noting, based on thermogravimetric analysis (TGA), the decomposition temperature (at 5% weight loss) for HexLQPH (372 °C) is ≈20 °C higher than HexLQPME (Figures S9 and S10, Supporting Information).

2.5. Thin Film Morphology by Atomic Force Microscopy (AFM)

Employing AFM, we probed the surface morphology of ≈40 nm thick films of HexLQPH:C_{60} and HexLQPME:C_{60} to investigate the role of hydrogen bonding on film formation and phase separation. Height images as well as phase images, which probe the local stiffness of the film surface, are shown in **Figure 4** for 3:2 blends of each compound. HexLQPME:C_{60} and HexLQPH:C_{60} films have RMS surface roughnesses of 1.2 and 0.3 nm, respectively (Figure 4a,b). The phase image of the HexLQPME:C_{60} surface (see Figure 4c) reveals that it is composed of round or oval-shaped domains that are 20–25 nm across surrounded by a random, interconnected mesh of the other phase, and the clear bimodal distribution of the AFM phase angle (see Figure 4e) agrees with phase separation into donor-rich and acceptor-rich domains typically observed in common photovoltaic donor and acceptor blends. On the other hand, intermixing of HexLQPH and C_{60} yields significantly less phase contrast as compared to the HexLQPME:C_{60} blend (see Figure 4d). The very narrow distribution of the AFM phase angle (see Figure 4e) suggests the molecular level mixing of HexLQPH and C_{60} in the in-plane directions. The result is consistent with HexLQPH forming closed/finite H-bonded assemblies that effectively limit the growth of donor domains to only 1D, i.e., the π-stacking direction.[59,63,66] The featureless HexLQPH:C_{60} film surface under AFM further suggests that the π-stacking direction of the HexLQPH donor assemblies is perpendicular to the surface, which is desirable for achieving efficient transport of photogenerated carriers toward the electrodes.

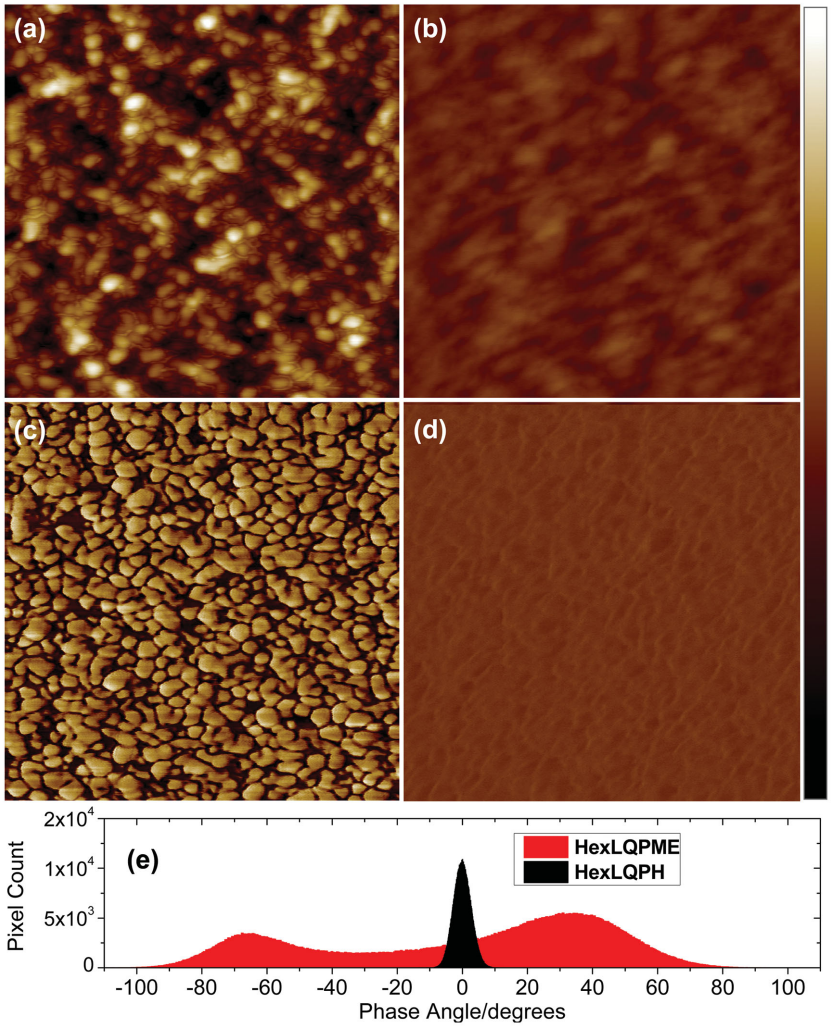

Figure 4. AFM images of ≈40 nm thick 3:2 blends of a,c) HexLQPME:C_{60} and b,d) HexLQPH:C_{60} deposited on Si substrates precoated with an 8 nm thick thermally evaporated MoO_3 layer; a,b) height images with a full scale of 7.5 nm and c,d) phase images with a full scale of −110° to +110°. The scale bar is shown to the right. a–d) 500 × 500 nm in size. e) A histogram comparing the distribution of the pixel values from phase images (c) and (d).

AFM height images of neat HexLQPH and HexLQPME films (Figures S11a,c, Supporting Information) show surfaces covered in nanoscale aggregates with RMS roughnesses of 0.5 and 1.9 nm, respectively. The typical lateral aggregate size is smaller for HexLQPH (20–40 nm) than for HexLQPME (30–70 nm). Furthermore, after annealing for 5 min at 100 °C, the HexLQPH surface is unchanged, while the HexLQPME aggregates grow to 70–150 nm across (Figure S11b,d, Supporting Information). Similar behavior is observed for HexLQPH:C_{60} and HexLQPME:C_{60} blends upon thermal annealing (Figures S12 and S13, Supporting Information). Again, the HexLQPH:C_{60} surface is unaffected by annealing, while the HexLQPME:C_{60} surface shows a simultaneous reduction in phase contrast and an increase in lateral domain size from 30–50 nm before annealing to 50–80 nm after annealing. Thus, H-bonding between HexLQPH molecules results in a locked morphology which does not change with thermal annealing at 100 °C, while HexLQPME molecules move much more freely and reorganize when thermal energy is supplied. This difference provides evidence that H-bonding in the HexLQPH films competes strongly with π–π stacking, and thus is a dominant force for directing morphology.

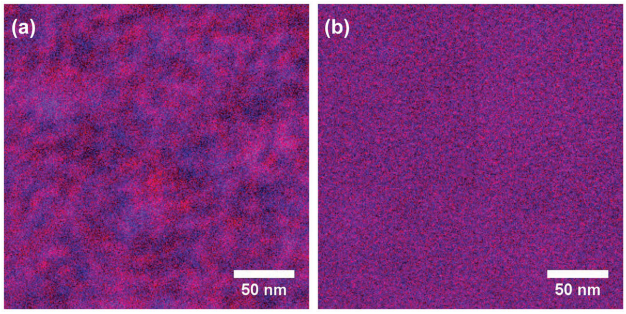

Figure 5. Energy filtered TEM images of a) HexLQPME:C_{60} and b) HexLQPH:C_{60}.

2.6. Thin Film Morphology by TEM

To confirm the above AFM results and further probe the degree of phase separation in HexLQPH:C_{60} and HexLQPME:C_{60} films, we employed energy filtered TEM imaging. For each composite image shown in **Figure 5**, two energy filtered images were taken sequentially at the same location on the film—the first image filtered with an electron energy loss of 19 ± 5 eV and the second image filtered with an electron energy loss of 30 ± 5 eV. Composite images were formed using the open source software ImageJ,[67] with red corresponding to bright areas from the 19 ± 5 eV (donor) image and blue corresponding to the bright areas from the 30 ± 5 eV (acceptor) image. In agreement with AFM results (vide supra), phase separated donor and acceptor domains are clearly visible in the HexLQPME:C_{60} film (Figure 5a) with a typical lateral size of 20–60 nm. Again, the HexLQPH:C_{60} film (Figure 5b) looks quite uniform, and thus we conclude that any phase separation that occurs in this blend is at a very small length scale, on the order of a few molecular lengths across. Traditional TEM images of neat HexLQPH and HexLQPME films are also shown in Figure S14 (Supporting Information). The neat HexLQPH film looks quite uniform, while grain boundaries are visible in the neat HexLQPME film, suggesting the growth of crystalline domains.

2.7. Grazing Incidence Wide Angle X-Ray Scattering (GIWAXS)

To probe molecular orientation in these films, we employed GIWAXS measurements on the neat and mixed films. As shown in **Figure 6**, GIWAXS patterns for neat films of HexLQPH and HexLQPME both show a partial arc of scattering corresponding to preferentially oriented π-stacking normal to the substrate in the case of HexLQPH (Figure 6d), and parallel to the substrate in the case of HexLQPME (Figure 6a). This orientation effect is highlighted in the arc profiles shown in Figure S15a (Supporting Information) (diffuse background subtracted), which shows that the π-stacking directions for the HexLQPH stacks are preferentially within 30° of the substrate normal direction, whereas that for the HexLQPME stacks are preferentially within 30° of the substrate surface plane. Additionally, radial profiles shown in Figure S15d (Supporting Information) indicate a 0.6 Å smaller average π-stacking distance for vertically oriented HexLQPH stacks (q_m = 16.6 nm^{-1}, or d = 3.8 Å) relative to laterally oriented HexLQPME stacks (q_m = 14.3 nm^{-1}, or d = 4.4 Å).

GIWAXS patterns for films blended with C_{60} (3:2 donor:C_{60}, 50 nm, Figure 6b,e) show similar features as the neat films discussed above, with the addition of an extra halo having a smaller radius centered at q_m = 6.8 nm^{-1} (d = 9.0 Å) consistent with C_{60} packing—the diameter of one C_{60} molecule is ≈8 Å.[68] The preferential orientation of π-stacking for both HexLQPH and HexLQPME remains after the addition of C_{60}, although this directionality becomes more diffuse, as indicated by the smaller angle-dependent intensity variation shown in the corresponding arc profiles (see Figure S15b in the Supporting Information). Nevertheless, radial profiles of the blend films shown in Figure S15e (Supporting Information) indicate a 0.7 Å smaller average π-stacking distance for vertically oriented HexLQPH stacks (q_m = 16.5 nm^{-1}, d = 3.8 Å) than that for the laterally oriented HexLQPME stacks (q_m = 14.0 nm^{-1}, d = 4.5 Å). Additionally, we note that the average π-stacking distance for randomly oriented HexLQPH domains in the HexLQPH:C_{60} blend is greater (q_m = 13.4 nm^{-1}, d = 4.7 Å) than for the vertically oriented domains, and matches the π-stacking distance observed for HexLQPME.

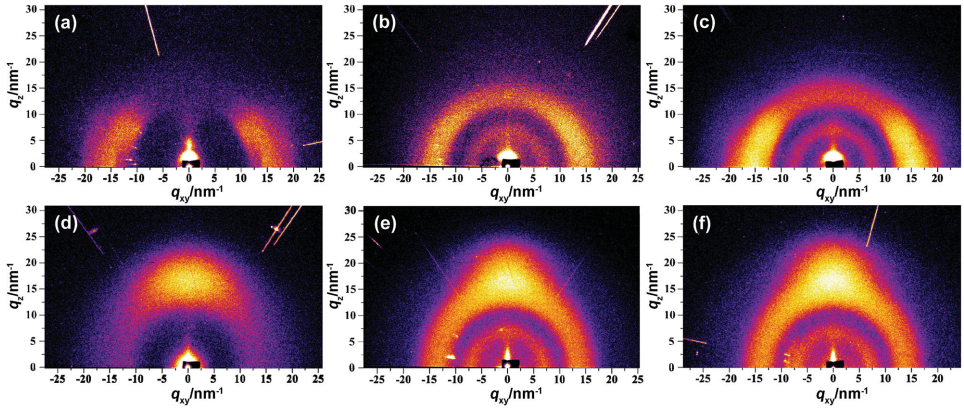

Figure 6. GIWAXS patterns for a) 30 nm neat HexLQPME, b,c) 50 nm HexLQPME:C_{60}, d) 30 nm neat HexLQPH, and e,f) 50 nm HexLQPH:C_{60}. b,e) For as-deposited films and c,f) for films annealed at 100 °C for 5 min in an N_2 glovebox. All blends have a 3:2 donor:C_{60} ratio.

Finally, we measured the GIWAXS patterns of the same blended films (3:2 donor:C_{60}, 50 nm) after thermal annealing in an N_2 glovebox for 5 min at 100 °C, shown in Figure 6c,f. Consistent with the AFM results, we see a significant increase in degree of orientation and scattered intensity after annealing the HexLQPME:C_{60} while the HexLQPH:C_{60} film is only weakly affected by annealing. As shown in the arc profiles in Figure S15c (Supporting Information), after annealing, the degree of orientation of HexLQPH decreases slightly while it increases substantially for HexLQPME domains in the annealed blend showing a much stronger tendency to align with the substrate surface.

Hence from the GIWAXS results, we conclude that the H-bonding directed assembly of HexLQPH results in vertically oriented and more tightly packed π-stacks, whereas in the absence of H-bonding, HexLQPME molecules preferentially orient edge-on to the substrate with π-stacks extending laterally. Such preferential orientations of the π-stacks are maintained with the addition of C_{60} molecules in the films, although the degree of preferential orientation is somewhat reduced. The susceptibility of these mixed films to thermally induced morphological changes can also be correlated with the different molecular orientations: with its π-stacking direction preferentially oriented parallel with the substrate surface, the HexLQPME stacks have an opportunity to grow through favorable π–π interactions into relatively large lateral domain sizes that tend to grow even larger under thermal annealing; on the other hand, no strong lateral interactions exist among the vertically oriented HexLQPH trimer stacks, which results in isolated vertical HexLQPH stacks with the fullerene molecules decorated in between, a picture consistent with the AFM results discussed above.

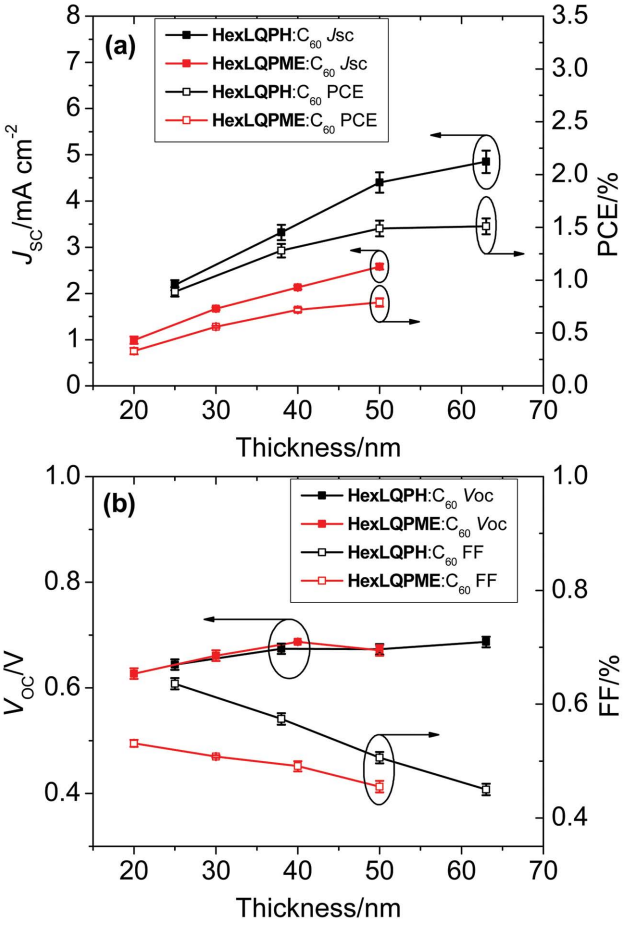

Figure 7. Photovoltaic performance for a series of BHJ active layer thicknesses of HexLQPH:C_{60} and HexLQPME:C_{60} devices: a) short-circuit current density (J_{SC}) and power conversion efficiency (PCE) and b) open-circuit voltage (V_{OC}) and fill factor (FF).

2.8. Organic Photovoltaic Device Performance of the LQ Derivatives

Photovoltaic devices were fabricated to further investigate how PH self-assembly affects the optoelectronic properties of HexLQPH films blended with C_{60}. The BHJ active layer for all devices was a 3:2 weight ratio of donor:C_{60} deposited by thermal evaporation at 10^{-6} Torr, and sandwiched between an ITO/MoO_3 (8 nm) anode and a bathocuproine (BCP, 8 nm)/Al cathode. Rough optimization of the blend ratio showed that 3:2 HexLQPH:C_{60} gave the best device efficiency (see Figure S16 and Table S3 in the Supporting Information), and this ratio was used for all further experiments. Finished devices were characterized in air with no encapsulation under simulated AM1.5G illumination from an Xe-arc lamp.

Comparison of device performance for HexLQPME:C_{60} and HexLQPH:C_{60} with varying active layer thickness are shown in **Figure 7** and summarized in Table S4 (Supporting Information) (data for a 50 nm active layer is also shown in **Table 2**). While the open-circuit voltage (V_{OC}) of these devices are very similar, as expected from electrochemical measurements, the short-circuit current (J_{SC}) is dramatically improved for the HexLQPH devices. The FF of the 50 nm thick HexLQPH devices is improved by 13% relative to the corresponding HexLQPME device, while the FF difference increases to greater than 20% at lower BHJ thicknesses. Overall, the efficiency of devices fabricated from HexLQPH is a factor of ≈2 times higher than that of the HexLQPME devices across the thickness range studied.

Insight into the source of the efficiency enhancement for the H-bond capable linear quaterthiophene was achieved by examining the EQE spectra and the current–voltage characteristics (Figure S17, Supporting Information). While the 50 nm thick HexLQPME:C_{60} device shows a peak EQE of 41% at λ = 425 nm, the 50 nm thick HexLQPH:C_{60} device shows an enhanced, redshifted EQE peaking at 64% and λ = 455 nm. Clearly, the redshifted absorption by HexLQPH as compared to HexLQPME (see Figure 2) contributes partially to the different EQE spectra observed here. Moreover, from the voltage dependencies of the photocurrent in these cells, we can extract the characteristic charge collection length L_C for the mixed layers by modeling the charge collection efficiency for photogenerated carriers at a given applied bias V as shown in Equation (1)[69,70]

$$\eta_{CC}(V) = \frac{L_C(V)}{d_m}\left[1-\exp\left(-\frac{d_m}{L_C(V)}\right)\right] \quad (1)$$

Table 2. OPV device characteristics based on HexLQPH, HexLQPME, MeBQPH, and MeBQPME.

Donor[a)]	V_{OC} [V]	J_{SC} [mA cm^{-2}]	FF [%]	PCE [%]	J_{SC} from EQE[b)] [mA cm^{-2}]	L_C (0 V) [nm]
HexLQPH:C_{60}	0.67 ± 0.01	4.4 ± 0.2	51 ± 1	1.49 ± 0.07	4.5	104
HexLQPME:C_{60}	0.67 ± 0.01	2.6 ± 0.1	46 ± 1	0.79 ± 0.05	2.6	32
MeBQPH:C_{60}	0.86 ± 0.01	3.0 ± 0.2	46 ± 1	1.20 ± 0.06	3.0	59
MeBQPME:C_{60}	0.90 ± 0.01	1.7 ± 0.1	37 ± 1	0.55 ± 0.05	1.7	34
HexLQPH:C_{70}	0.70 ± 0.01	6.6 ± 0.2	48 ± 1	2.24 ± 0.05	6.6	48
HexLQPME:C_{70}	0.71 ± 0.01	3.8 ± 0.1	32 ± 1	0.88 ± 0.05	3.9	21

[a)]All devices have the same structure with a 40 nm (MeBQPH, MeBQPME) or 50 nm (HexLQPH, HexLQPME) active layer and a 3:2 blend ratio (by weight) with C_{60} or 1:1 blend ratio with C_{70}. OPV device performance under 1 sun AM1.5G illumination: open-circuit voltage (V_{OC}), short-circuit current density (J_{SC}), fill factor (FF), power conversion efficiency (PCE), charge collection length (L_C), and charge collection efficiency (η_{CC}); [b)]J_{SC} determined by integration of EQE spectra assuming illumination with a perfect AM1.5G light source.

where d_m is the mixed layer thickness. From the fits shown in Figure S18 (Supporting Information) and the fitting results summarized in Table S4 (Supporting Information), we obtain a short-circuit L_c value (consistent across multiple layer thicknesses) of 29 ± 5 nm for HexLQPME:C_{60} and 102 ± 5 nm for HexLQPH:C_{60}. Thus, H-bonding mediated assembly of HexLQPH leads to an increase in absorption and charge collection efficiencies in the blend.

2.9. Comparing the Organic Photovoltaic Device Performance of the BQ and LQ Derivatives

Devices fabricated with the LQ donors were then compared to those of BQ as shown in **Figure 8** and summarized in Table 2. In general, the LQ devices show lower V_{OC}, but higher J_{SC} and FF than the BQ devices. V_{OC} has been shown to scale with the so-called interface gap between donor HOMO and acceptor LUMO in organic solar cells.[71] The ≈200 mV difference in V_{OC} corresponds to the ≈200 meV difference in the HOMO levels of BQ versus LQ, as measured by DPV (Table 1), with the deeper HOMO level of the BQ donors resulting in a greater V_{OC}. At the same time, the smaller HOMO–LUMO gap of the LQ molecules results in a redshifted absorption onset, which is partially responsible for the improved J_{SC}. Other contributions to the improved J_{SC} reside in the structural differences between the two molecules. The planarity of the LQ donor affords tighter π–π stacking, increasing the chromophore density, and leading to a higher absorption coefficient relative to that of BQ. The higher peak EQE for the HexLQPH device (62%) than the MeBQPH device (50%) is closely related to the nearly doubling of the short-circuit charge collection length (104 nm for the HexLQPH device versus 59 nm for the MeBQPH device, see Table 2). Considering that the formation of the donor stacks for efficient hole transport requires favorable π–π stacking among the H-bonded donor trimer assemblies, we attribute these differences to the planarity of the LQ and BQ chromophores as the more planar LQ chromophore is expected to facilitate the vertical π-stacking of donor domains.

Despite the above mentioned differences, the changes in device performance caused by the addition of H-bonding capability to the donor molecule are remarkably similar between the LQ and BQ systems. In both cases, the H-bonding promotes π-stacked aggregation of donor molecules, resulting in improved J_{SC} and FF, greatly increased charge collection length, and enhanced, redshifted EQE. These trends reinforce

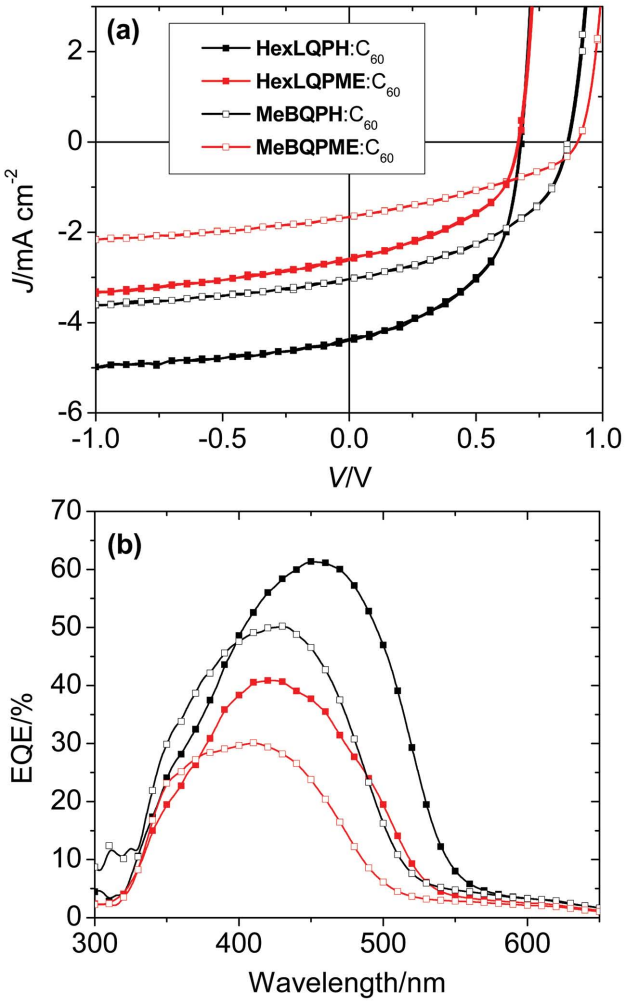

Figure 8. Comparison of device performance for 40–50 nm thick BHJ devices made from branched quaterthiophene donors (MeBQPH, MeBQPME, open symbols) and linear quaterthiophene donors (HexLQPH, HexLQPME, filled symbols). a) Current density (J) versus voltage (V) characteristics under 1 sun AM1.5G illumination and b) external quantum efficiency (EQE) spectra.

that H-bond promoted self-assembly is a promising strategy for molecular design to improve photovoltaic device performance.

Devices were also tested after thermal annealing for 5 min at 100 °C in an inert N_2 environment (see Figure S19 in the Supporting Information). For both HexLQPH:C_{60} and HexLQPME:C_{60} devices, the values of V_{OC} and J_{SC} were found to decrease slightly upon thermal annealing. However, the FF for HexLQPH:C_{60} increased after annealing, while the opposite was true for HexLQPME:C_{60}. Overall, and in agreement with the AFM results (vide supra), thermal annealing resulted in a significant reduction in PCE for the HexLQPME:C_{60} device while the performance was nearly unchanged for the HexLQPH:C_{60} device under the same annealing conditions.

2.10. Opportunities for Further Efficiency Improvement

The HexLQPH:C_{60} devices discussed above show a maximum EQE of 64% (at λ = 455 nm), which is close to that for many state-of-the-art high-efficiency OPV cells (with randomly phase separated BHJs), although the overall PCE for the HexLQPH based device is limited to only ≈1.5%.

Recognizing the need to improve long wavelength absorption, we have also fabricated devices using C_{70} as the acceptor, which has improved absorption in the visible region relative to C_{60}. As shown in **Figure 9** (also summarized in Table 2), the substitution of C_{70} for C_{60} results in an increase in J_{SC} by ≈50% for both the HexLQPH and HexLQPME devices, due to the long-wavelength contribution of C_{70} out to λ = 700 nm. We note that at these longer wavelengths the EQE is still higher for HexLQPH:C_{70} (EQE = 38% at λ = 500 nm) than it is for HexLQPME:C_{70} (EQE = 22% at λ = 550 nm) at wavelengths at which there is negligible donor absorption. This leads to a maximum PCE of 2.24% for the HexLQPH:C_{70} device, representing an ≈50% increase from that of the corresponding C_{60} device (1.49%). This further confirms that the morphology resulting from H-bonding not only improves absorption, but also charge collection efficiency. In progress is the development of lower-gap, solution-processable donor chromophores to better harvest longer wavelength solar radiation and tune the donor–acceptor energy level offsets for higher photovoltage output, a strategy which has been actively studied in the OPV community in recent years.[5] In the design of solution-processable molecules which assemble into supramolecular structures, the placement of solubilizing groups on the molecule will be critical to device performance, as discussed in the recent work of Yagai et al.[54] Further improving the EQE will likely also require designing planar donor chromophores that enable the robust formation of ordered donor domains (vertical stacks) with longer charge collection length. This will allow the BHJ layer thickness to be increased to achieve more complete light harvesting and/or an increase in the fill factor of the OPV devices.

3. Conclusions

We have demonstrated a self-assembly strategy to improve BHJ organic solar cell performance by introducing self-complementary hydrogen-bonding units to conventional quarterthiophene donor chromophores. We systematically compared the

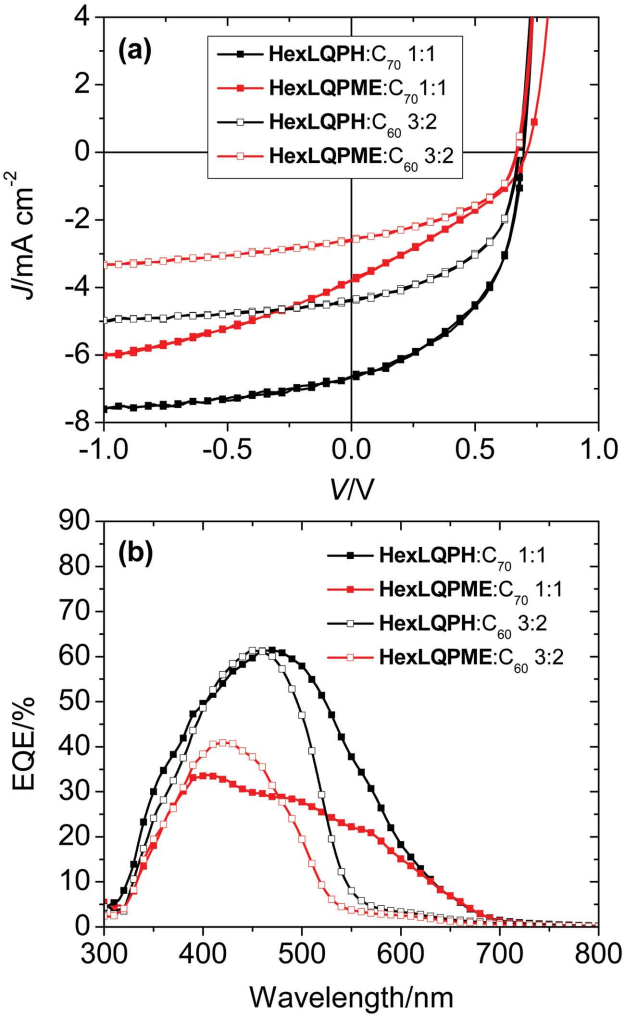

Figure 9. Comparison of devices incorporating C_{60} or C_{70} as the acceptor material: a) current density versus voltage characteristics under simulated 1 sun AM1.5G illumination and b) EQE spectra.

optoelectronic properties of HexLQPH to an H-bonding inactive comparator molecule HexLQPME, and then this pair to a branched quaterthiophene (BQ) family. In the molecularly dissolved state, HexLQPH and HexLQPME have nearly identical absorption behavior and HOMO/LUMO levels. However, consistent with the previously reported BQ system (e.g., MeBQPH and MeBQPME),[46] H-bonding induced aggregation of HexLQPH in solid films leads to enhanced, redshifted absorption. Combined morphological and structural characterization results from AFM, TEM, and GIWAXS reveal that the H-bonded HexLQPH donors preferentially form vertically oriented π-stacks with suppressed lateral aggregation whereas the HexLQPME comparators preferentially form laterally oriented π-stacks extending to over 30 nm in size that further grow with thermal annealing. Furthermore, the H-bonding induced ordering of HexLQPH π-stacks is retained in films blended with C_{60}, leading to twofold improved solar cell performance relative to HexLQPME blends. The H-bond capable donor shows a high maximum EQE of 64% with a short-circuit charge collection length of over 100 nm. The performance speaks to

the favorable morphology of, and charge transport within, the HexLQPH:C_{60} blended films that results from synergy between lateral H-bonding interactions and vertical π-stacking among the donor chromophores. In future work, we plan to extend the strategy to lower bandgap chromophores in order to more efficiently harvest the solar spectrum and yield higher photovoltage outputs.

4. Experimental Section

General Synthetic Methods and Molecular Characterization: Reagents and solvents were purchased from commercial sources and used without further purification unless otherwise specified. CH_2Cl_2 and DMF were degassed in 20 L drums and passed through two sequential drying columns (activated alumina for CH_2Cl_2; molecular sieves for DMF) under a positive argon atmosphere. 2-(5′-Hexyl-[2,2′-bithiophen]-5-yl)-4,4,5,5-tetramethyl-1,3,2-dioxaborolane **6**, 2-(tributylstannyl)thiophene, and tetrakis(triphenylphosphine)palladium(0) were purchased from Sigma-Aldrich and used as received. Dimethyl 4-bromophthalate **1** was prepared according to a literature procedure.[46] Thin layer chromatography (TLC) was performed on SiO_2-60 F_{254} aluminum plates with visualization by UV light or staining. Flash column chromatography was performed using silica gel technical grade, pore size 60 Å, 230–400 mesh particle size, 40–63 µm particle size from Sigma-Aldrich. 500 (125) MHz ^{1}H (^{13}C) NMR were recorded on an INOVA 500 spectrometer. Chemical shifts (δ) are given in parts per million (ppm) relative to TMS and referenced to residual protonated solvent purchased from Cambridge Isotope Laboratories, Inc. ($CDCl_3$: δ_H 7.26 ppm, δ_C 77.16 ppm; DMSO-d_6: δ_H 2.50 ppm, δ_C 39.52 ppm). Abbreviations used are s (singlet), d (doublet), t (triplet), q (quartet), quin (quintet), hp (heptet), b (broad), and m (multiplet). DART-TOF-MS spectra were recorded on an Agilent 6210 TOF spectrometer with MassHunter software. Elemental analyses were performed on a Carlo Erba-1106 instrument. Synthetic details can be found in the Supporting Information.

Thermal Analysis: TGA was performed using a TA Instruments TGA Q5000-0121 V3.8 Build 256 at a heating rate of 20 °C min^{-1} using 1–3 mg of sample in a 100 µL platinum pan (under nitrogen). The data were analyzed on Universal Analysis 2000 4.4A software. DSC was performed using a TA Instruments DSC Q1000-0620 V9.9 at a heating/cooling rate of 20–30 °C min^{-1} using 1–3 mg of sample in a sealed aluminum pan, with respect to an empty aluminum reference pan. Two cycles of heating and subsequent cooling were performed. The data were analyzed on Universal Analysis 2000 4.4A software.

Absorption Measurements: Solution absorption spectra were obtained using a Cary 100 Bio spectrophotometer, DMF as the solvent, and an Infrasil spectrophotometric 1 mm cuvette (Starna Cells, Inc.). All solvents were spectrophotometric grade and purchased from Sigma-Aldrich. Thin film absorption measurements were carried out with a calibrated Newport 818-UV Si photodiode illuminated by a Newport Oriel Apex illuminator and monochromator system chopped at 400 Hz. The signal was detected using a Stanford Research Systems SR830-DSP lock-in amplifier.

FT-IR Spectroscopy: Samples were prepared via vacuum deposition (10^{-6} Torr) onto NaCl salt plates (1 in. × 1 in.). Film thicknesses were the same as those used for device characterization. Spectroscopy was performed on a Bruker 80v FT-IR Spectrometer with OPUS v6.5 software or a Perkin Elmer Spectrum One spectrometer with Spectrum v5.0.1 software.

Cyclic Voltammetry (CV) and DPV: CV and DPV measurements were performed using a single-compartment three-electrode cell under argon blanket with a platinum flag as the counter electrode, a silver wire quasi-reference electrode calibrated versus Fc/Fc^+ in 0.1 M $TBAPF_6$ acetonitrile solutions ($E_{1/2}$ (Fc/Fc^+) = 0.10 V vs Ag/Ag^+), and a platinum disk (0.02 cm^2) as the working electrode. Tetrabutylammonium hexafluorophosphate ($TBAPF_6$) was purchased from Aldrich, recrystallized twice from absolute ethanol and dried under vacuum. DMF was collected from an Innovative Technologies solvent system, sparged with Ar, and passed over two columns of 5 Å activated sieves. The oligomer was dissolved to a concentration of 3.5×10^{-3} M in a 0.1 M $TBAPF_6$/DMF electrolyte. A voltammetric analyzer potentiostat/galvanostat was used under the control of BAS CV 50W software from Bioanalytical Systems. The scan rate for CV was 50 mV s^{-1}.

Vacuum Deposition: Films used for solid-state characterization, including photovoltaic devices, were deposited by vacuum thermal sublimation in a chamber pumped down to $<3 \times 10^{-6}$ Torr. Thicknesses were monitored during deposition using a calibrated quartz crystal monitor.

Thickness Determination: Film thicknesses were calibrated using a Dektak profilometer to measure the depth of a trench resulting from an ≈0.5 mm wide shadow mask. The thickness determined by the profilometer was then used to calibrate the quartz crystal monitor for subsequent depositions, resulting in an accuracy within ≈10% for films down to a few nm thickness.

Thin Film Characterization: AFM was carried out using a Veeco Innova AFM in tapping mode with a silicon tip (radius ≈8 nm) at 325 kHz with a force constant of ≈40 N m^{-1}. TEM samples were examined in a Zeiss Libra 120 equipped with in-line Omega filter at 120 kV. GIWAXS measurements were carried out on an Anton Paar SAXSess *mc*^{2} equipped with a multipurpose VarioStage. The scattered beam was recorded on an imaging plate (Multisensitive Storage Phosphor) and read using a Perkin Elmer cyclone 2D imaging plate reader. For the GIWAXS measurements, X-ray was generated at 40 kV/50 mA and the X-ray beam wavelength was $\lambda = 1.541$ Å (Cu Kα radiation). The incidence angle for the measurements was 0.2°.

Photovoltaic Device Performance Characterization: Devices were characterized under illumination from a 150 W Xe-arc lamp solar simulator with a KG1 filter, calibrated to 1 sun intensity using the AM1.5G spectrum with the spectral mismatch factor corrected. External quantum efficiency measurements were carried out with a calibrated Newport 818-UV Si photodiode illuminated by a Newport Oriel Apex illuminator and monochromator system chopped at 400 Hz. The signal was detected using a Stanford Research Systems SR830-DSP lock-in amplifier.

Theoretical Methodology: For all calculations the hexyl (Hex) solubilizing group was abbreviated to methyl (Me); independent experimental work has confirmed that this change does not have a significant influence on molecular optical or electronic properties. An initial surface exploration of MeLQPH as its lactam–lactam (NH/NH) tautomer was performed using a molecular mechanics molecular dynamics (MM MD) approach to identify the lowest energy conformation at room temperature. The initial structure was built using the Molden v. 5.0 software[72] and geometry optimized at the B3LYP/6-31+G* level of theory using the Gaussian 09 package.[73] The energy minimized structure was used as the input for the MM MD conformational space exploration. Partial atomic charges were obtained from the RESP charges of the B3LYP/6-31+G* geometry optimization. The S—C═C—S dihedral parameters describing the torsion angle between α-linked thiophene rings were obtained from a torsional exploration of 2,2′-bithiophene at the B3LYP/cc-pVTZ level of theory (see Figure S20 in the Supporting Information). Other dihedral parameters and angles were taken from the GAFF force field.[74] The energy minimized structure and parameters were fed into the Leap module of the AMBER 12 suite.[75] Newton's equations were integrated with a time step of 2 fs. The initial structure was minimized and the resulting coordinates were heated from 0 to 300 K for 2.5 ns. Finally, 200 ns of MM MD production were performed for every system with snapshots taken every 200 ps. Each snapshot was then minimized using MM. A clustering analysis over 1000 structures was performed using the ptraj module in the AMBER 12 suite. For one representative structure of every cluster, a geometry optimization was then performed at the B3LYP/6-31+G* level of theory which incorporated the polarizable continuum model (PCM) to compensate for solvent effects from DMF.[76] The 14 final structures and relative energies are provided in Figure S21 (Supporting Information). After identification of the low energy backbone structure of MeLQPH, the energies of the four NH/OH tautomers were established (Table S5, Supporting Information),

and the low energy conformation of MeLQPME was computed. Analogous calculations to the ones described above were performed to identify the low energy form of MeBQPH (Table S6, Supporting Information) and MeBQPME.

Supporting Information

Supporting Information is available from the Wiley Online Library or from the author.

Acknowledgements

R.K.C. acknowledges financial support from the National Science Foundation (CHE-1057411). J.X. and R.K.C. also acknowledge partial financial support from the Research Corporation for Science Advancement (Scialog Award No. 20316) and the University of Florida Office of Research. The authors thank University of Florida Research Computing for providing computational resources and support that have contributed to the research results are reported in this paper. The authors are also grateful to Prof. Kirk Schanze for providing access to the AFM instrumentation, and to Danielle Fagnani for assistance with the synthesis. TEM (J.C.) and GIWAXS (J.K.) experiments were conducted at the Center for Nanophase Materials Sciences (user project CNMS2014-286) at the Oak Ridge National Laboratory, which is a DOE Office of Science User Facility.

Received: May 1, 2015
Revised: June 24, 2015
Published online: July 20, 2015

[1] J. Xue, *Polym. Rev.* **2010**, *50*, 411.
[2] J. D. Myers, J. Xue, *Polym. Rev.* **2012**, *52*, 1.
[3] S. B. Darling, F. Q. You, *RSC Adv.* **2013**, *3*, 17633.
[4] N. Yeh, P. Yeh, *Renewable Sustainable Energy Rev.* **2013**, *21*, 421.
[5] W. Cao, J. Xue, *Energy Environ. Sci.* **2014**, *7*, 2123.
[6] K. A. Mazzio, C. K. Luscombe, *Chem. Soc. Rev.* **2015**, *44*, 78.
[7] Y. Huang, E. J. Kramer, A. J. Heeger, G. C. Bazan, *Chem. Rev.* **2014**, *114*, 7006.
[8] A. J. Heeger, *Adv. Mater.* **2014**, *26*, 10.
[9] A. K. K. Kyaw, D. H. Wang, C. Luo, Y. Cao, T.-Q. Nguyen, G. C. Bazan, A. J. Heeger, *Adv. Energy Mater.* **2014**, *4*, 1301469.
[10] K. Schmidt, C. J. Tassone, J. R. Niskala, A. T. Yiu, O. P. Lee, T. M. Weiss, C. Wang, J. M. J. Fréchet, P. M. Beaujuge, M. F. Toney, *Adv. Mater.* **2014**, *26*, 300.
[11] L. J. Richter, D. M. DeLongchamp, F. A. Bokel, S. Engmann, K. W. Chou, A. Amassian, E. Schaible, A. Hexemer, *Adv. Energy Mater.* **2015**, *5*, 1400975.
[12] H.-Y. Chen, J. Hou, S. Zhang, Y. Liang, G. Yang, Y. Yang, L. Yu, Y. Wu, G. Li, *Nat. Photonics* **2009**, *3*, 649.
[13] H. J. Son, W. Wang, T. Xu, Y. Liang, Y. Wu, G. Li, L. Yu, *J. Am. Chem. Soc.* **2011**, *133*, 1885.
[14] Y. Zhang, J. Zou, C.-C. Cheuh, H.-L. Yip, A. K.-Y. Jen, *Macromolecules* **2012**, *45*, 5427.
[15] S. Albrecht, S. Janietz, W. Schindler, J. Frisch, J. Kurpiers, J. Kniepert, S. Inal, P. Pingel, K. Fostiropoulos, N. Koch, D. Neher, *J. Am. Chem. Soc.* **2012**, *134*, 14932.
[16] J. Meiss, A. Merten, M. Hein, C. Schuenemann, S. Schäfer, M. Tietze, C. Uhrich, M. Pfeiffer, K. Leo, M. Riede, *Adv. Funct. Mater.* **2012**, *22*, 405.
[17] J. R. Tumbleston, A. C. Stuart, E. Gann, W. You, H. Ade, *Adv. Funct. Mater.* **2013**, *23*, 3463.
[18] A. C. Stuart, J. R. Tumbleston, H. Zhou, W. Li, S. Liu, H. Ade, W. You, *J. Am. Chem. Soc.* **2013**, *135*, 1806.
[19] L. Yang, J. R. Tumbleston, H. Zhou, H. Ade, W. You, *Energy Environ. Sci.* **2013**, *6*, 316.
[20] C.-Y. Chang, L. Zuo, H.-L. Yip, Y. Li, C.-Z. Li, C.-S. Hsu, Y.-J. Cheng, H. Chen, A. K.-Y. Jen, *Adv. Funct. Mater.* **2013**, *23*, 5084.
[21] H. Bronstein, J. M. Frost, A. Hadipour, Y. Kim, C. B. Nielsen, R. S. Ashraf, B. P. Rand, S. Watkins, I. McCulloch, *Chem. Mater.* **2013**, *25*, 277.
[22] J. W. Jo, J. W. Jung, H.-W. Wang, P. Kim, T. P. Russell, W. H. Jo, *Chem. Mater.* **2014**, *26*, 4214.
[23] S. Guo, J. Ning, V. Körstgens, Y. Yao, E. M. Herzig, S. V. Roth, P. Müller-Buschbaum, *Adv. Energy Mater.* **2015**, *5*, 1401315.
[24] J. W. Jo, S. Bae, F. Liu, T. P. Russell, W. H. Jo, *Adv. Funct. Mater.* **2015**, *25*, 120.
[25] J. Y. Lee, J. W. Jo, W. H. Jo, *Org. Electron.* **2015**, *20*, 125.
[26] J.-L. Wang, Q.-R. Yin, J.-S. Miao, Z. Wu, Z.-F. Chang, Y. Cao, R.-B. Zhang, J.-Y. Wang, H.-B. Wu, Y. Cao, *Adv. Funct. Mater.* **2015**, *25*, 3514.
[27] D. González-Rodríguez, A. P. H. J. Schenning, *Chem. Mater.* **2011**, *23*, 310.
[28] S. I. Stupp, L. C. Palmer, *Chem. Mater.* **2014**, *26*, 507.
[29] H.-L. Yip, H. Ma, A. K.-Y. Jen, J. Dong, B. A. Parviz, *J. Am. Chem. Soc.* **2006**, *128*, 5672.
[30] W. Hong, Z. Wei, H. Xi, W. Xu, W. Hu, Q. Wang, D. Zhu, *J. Mater. Chem.* **2008**, *18*, 4814.
[31] S. Yagai, T. Kinoshita, Y. Kikkawa, T. Karatsu, A. Kitamura, Y. Honsho, S. Seki, *Chem. Eur. J.* **2009**, *15*, 9320.
[32] Z. Wei, W. Hong, H. Geng, C. Wang, Y. Liu, R. Li, W. Xu, Z. Shuai, W. Hu, Q. Wang, D. Zhu, *Adv. Mater.* **2010**, *22*, 2458.
[33] M. Gsänger, J. H. Oh, M. Könemann, H. W. Höffken, A.-M. Krause, Z. Bao, F. Würthner, *Angew. Chem. Int. Ed.* **2010**, *49*, 740.
[34] Q. Tang, Z. Liang, J. Liu, J. Xu, Q. Miao, *Chem. Commun.* **2010**, *46*, 2977.
[35] Y. Suna, J.-I. Nishida, Y. Fujisaki, Y. Yamashita, *Chem. Lett.* **2011**, *40*, 822.
[36] M. Bonini, L. Zalewski, E. Orgiu, T. Breiner, F. Dötz, M. Kastler, P. Samorì, *J. Phys. Chem. C* **2011**, *115*, 9753.
[37] M. Irimia-Vladu, E. D. Głowacki, P. A. Troshin, G. Schwabegger, L. Leonat, D. K. Susarova, O. Krystal, M. Ullah, Y. Kanbur, M. A. Bodea, V. F. Razumov, H. Sitter, S. Bauer, N. S. Sariciftci, *Adv. Mater.* **2012**, *24*, 375.
[38] Y. Suna, J.-I. Nishida, Y. Fujisaki, Y. Yamashita, *Org. Lett.* **2012**, *14*, 3356.
[39] Z. He, D. Liu, R. Mao, Q. Tang, Q. Miao, *Org. Lett.* **2012**, *14*, 1050.
[40] E. D. Glowacki, L. Leonat, M. Irimia-Vladu, R. S. Diauer, M. Ullah, H. Sitter, S. Bauer, N. S. Sariciftci, *Appl. Phys. Lett.* **2012**, *101*, 023305.
[41] E. D. Głowacki, M. Irimia-Vladu, M. Kaltenbrunner, J. Gsiorowski, M. S. White, U. Monkowius, G. Romanazzi, G. P. Suranna, P. Mastrorilli, T. Sekitani, S. Bauer, T. Someya, L. Torsi, N. S. Sariciftci, *Adv. Mater.* **2013**, *25*, 1563.
[42] S.-M. Jeong, T.-G. Kim, E. Jung, J.-W. Park, *ACS Appl. Mater. Interfaces* **2013**, *5*, 6837.
[43] E. D. Głowacki, H. Coskun, M. A. Blood-Forsythe, U. Monkowius, L. Leonat, M. Grzybowski, D. Gryko, M. S. White, A. Aspuru-Guzik, N. S. Sariciftci, *Org. Electron.* **2014**, *15*, 3521.
[44] J. Yoshida, A. Ueda, A. Nakao, R. Kumai, H. Nakao, Y. Murakami, H. Mori, *Chem. Commun.* **2014**, *50*, 15557.
[45] J. Dhar, D. P. Karothu, S. Patil, *Chem. Commun.* **2015**, *51*, 97.
[46] B. M. Schulze, N. T. Shewmon, J. Zhang, D. L. Watkins, J. P. Mudrick, W. Cao, R. Bou Zerdan, A. J. Quartararo, I. Ghiviriga, J. Xue, R. K. Castellano, *J. Mater. Chem. A* **2014**, *2*, 1541.

[47] Z. Chen, V. Stepanenko, V. Dehm, P. Prins, L. D. A. Siebbeles, J. Seibt, P. Marquetand, V. Engel, F. Würthner, *Chem. Eur. J.* **2007**, *13*, 436.
[48] I. D. Tevis, W.-W. Tsai, L. C. Palmer, T. Aytun, S. I. Stupp, *ACS Nano* **2012**, *6*, 2032.
[49] R. J. Kumar, J. Subbiah, A. B. Holmes, *Beilstein J. Org. Chem.* **2013**, *9*, 1102.
[50] A. Ruiz-Carretero, T. Aytun, C. J. Bruns, C. J. Newcomb, W.-W. Tsai, S. I. Stupp, *J. Mater. Chem. A* **2013**, *1*, 11674.
[51] K. H. Lam, T. R. Foong, Z. E. Ooi, J. Zhang, A. C. Grimsdale, Y. M. Lam, *ACS Appl. Mater. Interfaces* **2013**, *5*, 13265.
[52] T. Aytun, L. Barreda, A. Ruiz-Carretero, J. A. Lehrman, S. I. Stupp, *Chem. Mater.* **2015**, *27*, 1201.
[53] F. Bruni, M. Sassi, M. Campione, U. Giovanella, R. Ruffo, S. Luzzati, F. Meinardi, L. Beverina, S. Brovelli, *Adv. Funct. Mater.* **2014**, *24*, 7410.
[54] S. Yagai, M. Suzuki, X. Lin, M. Gushiken, T. Noguchi, T. Karatsu, A. Kitamura, A. Saeki, S. Seki, Y. Kikkawa, Y. Tani, K.-I. Nakayama, *Chem. Eur. J.* **2014**, *20*, 16128.
[55] R. B. K. Siram, M. Stephen, F. Ali, S. Patil, *J. Phys. Chem. C* **2013**, *117*, 9129.
[56] A. Yassin, P. Leriche, M. Allain, J. Roncali, *New J. Chem.* **2013**, *37*, 502.
[57] K.-H. Kim, H. Yu, H. Kang, D. J. Kang, C.-H. Cho, H.-H. Cho, J. H. Oh, B. J. Kim, *J. Mater. Chem. A* **2013**, *1*, 14538.
[58] Z. Xiao, K. Sun, J. Subbiah, S. Ji, D. J. Jones, W. W. H. Wong, *Sci. Rep.* **2014**, *4*, 05701.
[59] A. Mourran, U. Ziener, M. Möller, M. Suarez, J.-M. Lehn, *Langmuir* **2006**, *22*, 7579.
[60] T. Kaseyama, S. Furumi, X. Zhang, K. Tanaka, M. Takeuchi, *Angew. Chem. Int. Ed.* **2011**, *50*, 3684.
[61] A. Mishra, P. Bäuerle, *Angew. Chem. Int. Ed.* **2012**, *51*, 2020.
[62] B. M. Schulze, D. L. Watkins, J. Zhang, I. Ghiviriga, R. K. Castellano, *Org. Biomol. Chem.* **2014**, *12*, 7932.
[63] X. Zhao, D. L. Watkins, J. Galindo, N. T. Shewmon, A. E. Roitberg, J. Xue, R. K. Castellano, S. S. Perry, *Org. Electron.* **2015**, *19*, 61.
[64] M. Pope, C. E. Swenberg, *Electronic Processes in Organic Crystals and Polymers*, Oxford University Press, New York **1999**.
[65] B. Morzyk-Ociepa, *J. Mol. Struct.* **2007**, *846*, 74.
[66] M. Suárez, J.-M. Lehn, S. C. Zimmerman, A. Skoulios, B. Heinrich, *J. Am. Chem. Soc.* **1998**, *120*, 9526.
[67] C. A. Schneider, W. S. Rasband, K. W. Eliceiri, *Nat. Methods* **2012**, *9*, 671.
[68] A. Goel, J. B. Howard, J. B. Vander Sande, *Carbon* **2004**, *42*, 1907.
[69] B. P. Rand, J. Xue, S. Uchida, S. R. Forrest, *J. Appl. Phys.* **2005**, *98*, 124902.
[70] J. Xue, B. P. Rand, S. Uchida, S. R. Forrest, *Adv. Mater.* **2005**, *17*, 66.
[71] A. Gadisa, M. Svensson, M. R. Andersson, O. Inganäs, *Appl. Phys. Lett.* **2004**, *84*, 1609.
[72] G. Schaftenaar, J. H. Noordik, *J. Comput.-Aided Mol. Des.* **2000**, *14*, 123.
[73] M. J. Frisch, G. W. Trucks, H. B. Schlegel, G. E. Scuseria, M. A. Robb, J. R. Cheeseman, J. J. A. Montgomery, T. Vreven, K. N. Kudin, J. C. Burant, J. M. Millam, S. S. Iyengar, J. Tomasi, V. Barone, B. Mennucci, M. Cossi, G. Scalmani, N. Rega, G. A. Petersson, H. Nakatsuji, M. Hada, M. Ehara, K. Toyota, R. Fukuda, J. Hasegawa, M. Ishida, T. Nakajima, Y. Honda, O. Kitao, H. Nakai, M. Klene, X. Li, J. E. Knox, H. P. Hratchian, J. B. Cross, V. Bakken, C. Adamo, J. Jaramillo, R. Gomperts, R. E. Stratmann, O. Yazyev, A. J. Austin, R. Cammi, C. Pomelli, J. W. Ochterski, P. Y. Ayala, K. Morokuma, G. A. Voth, P. Salvador, J. J. Dannenberg, V. G. Zakrzewski, S. Dapprich, A. D. Daniels, M. C. Strain, O. Farkas, D. K. Malick, A. D. Rabuck, K. Raghavachari, J. B. Foresman, J. V. Ortiz, Q. Cui, A. G. Baboul, S. Clifford, J. Cioslowski, B. B. Stefanov, G. Liu, A. Liashenko, P. Piskorz, I. Komaromi, R. L. Martin, D. J. Fox, T. Keith, M. A. Al-Laham, C. Y. Peng, A. Nanayakkara, M. Challacombe, P. M. W. Gill, B. Johnson, W. Chen, M. W. Wong, C. Gonzalez, J. A. Pople, *Gaussian 09, Revision D.01*, Gaussian, Inc., Wallingford, CT **2009**.
[74] J. Wang, R. M. Wolf, J. W. Caldwell, P. A. Kollman, D. A. Case, *J. Comput. Chem.* **2004**, *25*, 1157.
[75] D. A. Case, T. A. Darden, T. E. CheathamIII, C. L. Simmerling, J. Wang, R. E. Duke, R. Luo, R. C. Walker, W. Zhang, K. M. Merz, B. Roberts, S. Hayik, A. Roitberg, G. Seabra, J. Swails, A. W. Götz, I. Kolossváry, K. F. Wong, F. Paesani, J. Vanicek, R. M. Wolf, J. Liu, X. Wu, S. R. Brozell, T. Steinbrecher, H. Gohlke, Q. Cai, X. Ye, J. Wang, M.-J. Hsieh, G. Cui, D. R. Roe, D. H. Mathews, M. G. Seetin, R. Salomon-Ferrer, C. Sagui, V. Babin, T. Luchko, S. Gusarov, A. Kovalenko, P. A. Kollman, *AMBER 12*, University of California, San Francisco, CA **2012**.
[76] S. Miertuš, E. Scrocco, J. Tomasi, *Chem. Phys.* **1981**, *55*, 117.